

Phase Transition of Iron-based Single Crystals at Extreme Strain Rates under Dynamic Loadings

Kun Wang¹, Jun Chen^{1,2*}, Wenjun Zhu^{3*}, Wangyu Hu⁴, Meizhen Xiang¹

Phase transformation of iron from α to ϵ phase, as a prototype of solid-solid phase transition under dynamic loadings, has been researched from its thermodynamics and kinetics to its phase transition mechanism at lattice level over the past six-decade developments of experimental techniques and computation abilities. The transition pressure (TP) exhibit huge diverges among experiments with different pressure medium and loading rates, even in the same initial samples. Great achievements are made in understanding the strain or stress dependence of the TP. However, the underlying physics of the strain rate dependence are relatively less understood, even a virgin under extreme high strain rates, despite of some existing experimental laws. In this letter, the TP is found to depend on the strain rate because of nucleation time of the transition product, which is similar a scaling law albeit with a systematic error at extreme strain rates. Moreover, formation time of the initial shock, caused by the phase transition, also obey a scaling law under ramp compressions with different the strain rates. It is amazing that critical strain of lattice instability, happening before the phase transition, change at extreme strain rates, while be nearly a constant at relatively low strain rates. The change of the critical strain just corresponds the systematic error of the scaling law obey be the TP, which indicates a new physical effect at extreme strain rates. And the physical effects of the strain rates on the instability are well interpreted through the conception of strain gradient, which could only emerge at dynamic loadings.

Recent significant advancements on the ultrafast X-ray diagnostics ^{1, 2, 3, 4} under dynamic loadings has prompted a renewed interest in phase transformation of iron from α (bcc) to ϵ (hcp) phase — a prototype of solid-solid phase transition under high pressures. Numerical predictions on dynamic behaviors of materials in respond to dynamic loadings require knowing the dynamics of the phase transition. It is known that bcc \leftrightarrow hcp phase transition of iron under dynamic loadings happens at a metastable two-phase surface where the actual mass fraction of ϵ phase need a time, termed relaxation time, to develop to the one of thermodynamic equilibrium ⁵. An outstanding character of the metastable state is the “over-pressurization” beyond the equilibrium phase boundary at high strain rate. It is found that the relaxation time could relate to the over-pressurization approximately through an exponential function ⁶. Hence, the knowledge of the over-pressurization, or alternatively the onset of the phase transition, is critical to understanding the dynamics of the phase transition. Historically, the transition pressure (TP) of iron detected in different experiments varies from about 8 GPa to 25 GPa ⁷, which has been attributed to reasons of initial shear of samples⁸, pressure mediums ⁹ and local strain or stress states ¹⁰. Theoretical understandings of the strain or stress dependence of the TP have also been well achieved with mechanical instability criteria and thermal dynamic criteria, i.e., Born’s criteria ¹¹, or its modified version to include initial strain effects ¹², and common tangent constructions

¹ Laboratory of Computational Physics, Institute of Applied Physics and Computational Mathematics, Beijing 100088, PR China, ² Center for Applied Physics and Technology, Peking University, Beijing 100071, China, ³ National Key Laboratory of Shock Wave and Detonation Physics, Institute of Fluid Physics, Mianyang 621900, China, ⁴ College of Materials Science and Engineering, Hunan University, Changsha 410082, China. * Email: jun_chen@iapcm.ac.cn; wjzhu@caep.cn.

method^{7, 13}. However, recent experiments show that the TP exhibits a strong strain-rate ($\dot{\epsilon}$) dependence under extreme strain rate^{6, 14, 15, 16}, and a power law between them is approximately obeyed when $\dot{\epsilon} > 10^6 \text{ s}^{-1}$ ¹⁵, which is similar to the rate-dependence plastic flow observed in aluminum and iron governed by the dislocation flow mechanism¹⁷. Significant difficulties are encountered by the theories, developed under static conditions, when explaining the strain-rate dependence of the TP under dynamic loadings.

In contrast to traditional dynamic (shock) compressions, ramp compression is a kind of quasi-isotropic (QI) compression technique, which could generate a pressure range up to the order of terapascal in solid matter¹⁸. Because the pressure range is much larger than that produced by static high pressure techniques (such as diamond anvil cell), it is broadly employed in the matter research regime under extreme conditions^{18, 19, 20}. Combined with the shock compressions (a so-called shock-ramp compressions), different thermodynamic compression paths of materials, including the P-T region between the shock Hugoniot and isentrope, are allowed to be accessed and thus open a much wider thermodynamic space for materialists to explore^{21, 22}. Besides, the ramp compression is adopted for purpose of effective performances in inertially confined fusion implosions, either direct (ablative) or indirect (hohlraum) drive. Unfortunately, the ramp compression wave in materials is unstable, which will progressively steepen and finally forms a shock after a certain propagation distance. This means that only materials within the propagation distance before formation of the shock is under isotropic compressions. It is found that the solid-solid phase transition favors the shock formations during ramp compressions and results in deviations from expected thermodynamic path^{23, 24}, but the formation processes of the shock, as well as its underline physics, at lattice level are not clear at present.

In this letter, nonequilibrium molecular dynamics (NEMD) simulations, combined with a recently developed interatomic potential of iron²⁵, are conducted to study the effects of strain rates on the $\alpha \leftrightarrow \epsilon$ phase transition and its influence on the shock formation time under ramp compressions. The ramp compressions are performed by compressing an iron sample with a rigid wall which moves linearly from 0 km/s to v_{\max} (km/s) within a time of t_{rising} . For brevity, the applied strain rates ($\dot{\epsilon}$) and the loading condition, involving the peak particle velocity and the ramp rising time, are uniformly represented by $v_{\max}/t_{\text{rising}}$ due to the relation of $\dot{\epsilon} = \dot{v}_p/C = v_{\max}/(Ct_{\text{rising}})$, where C is the speed of elastic wave and \dot{v}_p is the time derivative of the particle velocity (v_p). We perform ramp compressions along [001] direction of perfect bcc iron at 0K, with a peak particle velocity of 0.8 km/s and a ramp rising time of 5, 10, 15 and 50 ps, respectively. As a comparison, another group of ramp compressions, consisting of three simulations, is performed by fixing the ramp rising time at 50 ps while increasing the maximum particle velocity from 0.8 to 1.5 km/s (that are 1.0, 1.2 and 1.5 km/s). The dimension of initial iron sample is 14.30×14.30×286.06 nm. A slightly enlarged iron sample, whose dimension is 17.16×17.16×286.06 nm, is employed for the second group of ramp compressions.

Wave profiles, represented by particle velocity (v_p) and ZZ component of local stresses, are calculated at several wave propagation time for different ramp compressions (See Fig. 1 and S1-3). The structure of the wave profile changes with the wave propagation time before a steady shock wave forms during ramp compressions. To understand the microscopic reasons behind the changes of the wave structure, spatial distributions of the first nearest neighbor separation distance (r_0) and coordination number along Z direction are analyzed at the time corresponding to that of the

particle velocity profiles (See Fig. 1). Calculation details could be found in the Methods and Supplementary Information. From the results shown Fig. 1-2, several features could be identified. First, homogeneous nucleation begins after bcc phase changes into a ten-coordination-number (TCN) structure during ramp compressions. That is to say, the hcp phase is transformed from the TCN structure rather than a bcc phase. The formation of the TCN structure is due to small relaxations of instable bcc phase via compressions along [001] direction within (110) or (1-10) plane and forming a hexagon pattern in these planes. The TCN structure is also observed before the phase transition in the shock upon single crystalline iron²⁵ where the TCN structure is corresponding to the result of the first step toward phase transition of iron from bcc to hcp phase. The change from compressed bcc phase to the TCN structure does not cause an apparent rising in temperature, while the transition from the TCN structure to hcp phase does (See S1). And the phase transition of iron makes the compression wave quickly become a shock. Second, the phase transition wave (TW), represented by the moving phase interface, proceeds in a region consisting of the TCN structure. For brevity, the region consisting of the TCN structure is called instability region and the boundary between the instability region and the bcc phase region is called instability boundary (IB) in present work. From snapshots of compressed iron sample shown in Fig. 2, nucleuses of hcp phase would be continually created in the instability region and later, be combined by the passing-by phase interface. The right boundary of the nucleation region, or NB for short, propagates faster than the IB in the early stage of ramp compressions, which would eventually catch up to the IB after a certain wave propagation time and thus form an initial shock. If the final particle velocity is large enough (as the case of present work), the TW would catch up to the NB after the initial shock forms, which results in a steady single shock wave. The formation time of the initial shock grows with the decreasing of the applied strain rates. Their relations will be built later in this letter. The whole formation processes of the final shock could be found in the Supplementary Information. The movement of the phase interface is driven by the growth of the transition products and the combinations with the nucleuses generated in the instability region. While the movement of the NB is driven via interactions between nucleation near the NB and the strain fields generated by nearby nucleus, which will be addressed further. From the above discussions, the phase transition at extreme strain rates happens in perfect bcc iron through two processes: lattice instability and nucleation. Thus, our remaining task of this letter is to study the rate dependence of the lattice instability and nucleation.

The TP as function of applied strain rates is shown Fig. 2a, where a power laws of the strain rate dependence (or a scaling law) is approximately obeyed. Similar power law is only observed in experiments¹⁵, which is attributed to thermal activation mechanism similar to that of plastic deformations of metals¹⁷. However, the mechanism does not work here because temperature keeps at its initial value (0 K) until the phase transition takes place (See Fig. 1). In present work, the strain rate dependence of the TP is due to the time needed to nucleate from bcc phase to an hcp nucleus. Under static compressions at 0K, single crystalline iron will begin to nucleate after the bcc phase is compressed to a critical strain, above which bcc iron is instable. While under high strain rates, the bcc phase does not have enough nucleation time (τ) to finish the transition from a bcc phase to an hcp nucleus so that it is carried into a higher stress state than the onset of instabilities. This means that the excess of strain ($\Delta\epsilon$) over the critical strain (ϵ_c) of the instability increases with growth of the applied strain rates by $\tau\dot{\epsilon}$, which lead to a strain-rate-dependence TP, i.e., $\sigma_{TP}(\epsilon_c + \tau\dot{\epsilon})$. The nucleation time is approximately proportional to v^{-1} , where v is optical

phonon frequency of compressed bcc cell at the onset of the instability. According to our simulation results, the critical strain at different strain rates are calculated and plotted as a function of strain gradient in Fig 2b. It is known that any strain rates, applied to a sample, will generate an additional strain gradient disturbance in the sample, which is the main difference from the static compressions. Because of the perfect bcc iron employed here, the emergence of the strain gradient field completely stems from the applied strain rates under dynamic loadings. The strain gradient distributions in response to the applied strain rates are given in the Supplementary Information. As shown in Fig. 2b, the critical strain is gradually decreases in its absolute value as the strain gradient (or strain rate) grows. However, a rate-independence critical strain is predicted by the traditional theories on the lattice instabilities (See Fig. 2c), which is corresponding to values when the strain gradient (or strain rate) approaches to zero. The obvious rate dependence of the critical strain under the large strain rates could be explained by contributions of the strain gradients to the energies of the bcc phase. Through reformulation the lattice stability condition to including the contributions of the strain gradients, we could obtain another group of stability condition, that is,

$$\tilde{T}_{ijklmn}\delta\tilde{\kappa}_{ijk}\delta\tilde{\kappa}_{lmn} \geq 0, \quad (1)$$

where

$$\tilde{T}_{ijklmn} = T_{ijklmn} + \frac{1}{2}(\Gamma_{ijklmn} + \Gamma_{lmnij k}), \quad (2)$$

$$\Gamma_{ijklmn} = (\tau_{ijm}\delta_{kn} + \tau_{imk}\delta_{jn} + \tau_{mjk}\delta_{in} - \tau_{ijk}\delta_{mn})\Delta a_l. \quad (3)$$

Higher than second-order terms of $\delta\tilde{\kappa}_{ijk}$ are neglected here. Δa_l is a measure of strain at the location of interest under strain gradient of $\boldsymbol{\kappa}$, which satisfies a relation of $\boldsymbol{\eta}(\mathbf{X}) = \nabla\boldsymbol{\eta}(\mathbf{X})\Delta\mathbf{a}$. $\boldsymbol{\tau}$ is a higher order stress conjugate to $\boldsymbol{\kappa}$, and δ_{ij} is a Kronecker delta. All subscripts in the above equations run from one to three. Detailed derivations could be found in the Methods. This condition requires $\tilde{\mathbf{T}}$ to be positive definite. It is convenient to contract the six indexes of $\tilde{\mathbf{T}}$ into two by the rules mentioned in the Methods where (ijk) or (lmn) could be mapped into one index which ranges from one to eighteen. Obviously, $\tilde{\mathbf{T}}$ is a symmetric matrix which has eighteen real eigenvalues. Then the conditions (1) require that the minimum eigenvalue is larger than zero. This condition enables us to know whether the crystal is stable at presences of strain gradient disturbances. To distinguish these two groups of stability conditions, we referred to condition (1) as gradient stability condition, and the condition derived from strain disturbance as strain stability condition in this letter. The final stability of a lattice should be determined by both of the two stability conditions. Hence, the instabilities of a crystal are a competing result between strain instabilities and gradient instabilities. As shown in Fig. 2d, the minimum eigenvalue (\tilde{T}_{min}) is calculated at different strain and strain gradient via lattice dynamic method mentioned in the Methods. The negative value of \tilde{T}_{min} means that bcc iron with strain gradient disturbances is less stable than the one without the disturbances. That is to say, the absolute value of the critical strain predicted by the strain stability condition would decrease at the presence of large gradient strain, which is consistent with the results shown in Fig 2b. However, the contributions of the strain gradient to the stabilities are much smaller than that of the strain at low applied strain rate because of the small strain gradient. According to the results shown in Fig. 2b, the contributions of the strain gradients cannot be neglected when the strain gradient is larger than $1.43\text{e-}4 \text{ \AA}^{-1}$, corresponding to the strain rates larger than 0.053 \AA/ps^2 in our simulations. Besides, although the critical strain decreases, additionally stresses, generated by the higher order stresses conjugate to the strain gradients, contribute to the TP under the extreme strain rates, which lead to an increasing

in the TP as observed in Fig. 3a.

Phase transition begins to nucleate at the instability region only when disturbance fields are present. The disturbance may be temperature fluctuations or additional strain field generated by newly forming lattice defects. Because the instability does not cause an apparent rising in temperature, the temperature of the instability region keeps zero until nucleation begins. Thus, temperature fluctuations are not the source of the disturbance here. We believe that the disturbances of a nucleation site are caused by strain fields generated by newly forming nucleuses nearby. And the generated strain fields will trigger the next nucleation farther away from the initial nucleation site. These processes are repeated as more and more nucleuses nucleate from the initial nucleation site to its surrounding and form the NB propagating in the instability region. According to this physical picture, the speed of the moving boundary of nucleation could be evaluated as follows. A schematic drawing of the nucleation of hcp phase has been shown in Fig. 4a, where the gray and black bars denote adjacent shuffle planes, i.e., (110) or (1-10), in bcc iron. Nucleation could begin either by consecutively shuffling layer by layer or simultaneously shuffling several layers at one time. Bertrand et. al.²⁶ compared the two transition path by *ab initio* calculations and found that the consecutive shuffle manner is more energetically favorable. However, more complex consecutive shuffle manners are not explored, for example, nucleation proceeds by shuffling two or more layers each time. Here, we assume the number of active layers is m during the nucleation, which relies on the distance between two adjacent shuffle planes, strain and its gradient at the nucleation site, as well as cutoff distance of the interaction potential. Every shuffle will move the phase interface forwards a distance of $2md$ along [110] (or [1-10]) direction, where d is the distance between two adjacent {110} planes, that is $\sqrt{2}a_0/2$, a_0 is lattice constant of bcc iron. Since the nucleation proceed in the instability region where nearly no energy barrier is needed to overcome during every try of the shuffle by atom layers, the try frequency of the shuffle is equal to optical phonon frequency (ν) along [110] or [1-10] direction in reciprocal space of compressed bcc lattice. Thus the moving speed of the phase interface along [110] (or [1-10]) is $2md\nu$. Because phase transition domain is always close to be ellipsoidal (See Fig. 4b), the moving speed of the phase interface along [001] direction is proportional to the speed along [110] (or [1-10]). Let χ_0 to be the ratio between the principal-axis lengths of the ellipsoidal along [110] (or [1-10]) and [001] at unstrained state (See Fig. 4b), the ratio at a compressed state, whose uniaxial compression ratio is λ , is $\lambda\chi_0$ for the first layer. Considering the present of a small strain gradient (κ), the uniaxial compression ratio at layer i relates to the one at layer 0 by $\lambda_i = \lambda_0 + id\kappa$. Thus the moving speed (U_{\parallel}) of the phase interface along [001] is

$$U_{\parallel} = 2\chi_0 d\nu \sum_{i=0}^{m-1} (\lambda_0 + id\kappa) + v_p, \quad (4)$$

where v_p , the mass center velocity of the nucleus, could be approximately evaluated by the average particle velocity at the nucleation position. Because movements of the boundary of the nucleation region are caused by the inter-triggering between nucleation and strain field disturbance, the resulting boundary speed is sum of the moving speed of the phase interface of new nucleuses and the propagation speed of strain field generated by the new nucleuses.

The time evolutions of strain ahead of the IB are shown in Fig. 4d, where the strain gradually decreases until the NB catches up to the IB to form the initial shock after a certain wave propagation time. And the absolute value of the final strain ahead of the IB grows with the increasing strain rate. We will discuss the shock formation condition and determine the shock formation time below. To achieve a transformation from bcc to hcp phase, the energy of the

compressed bcc phase should be large enough to enable a subsequence shuffle processes among $\{110\}$ planes. The bcc phases of different strain at the beginning of the instability region will transform into hcp phases with different initial strains. For example, the ideal transition path requires a compression ratio of 86.6% along $[001]$ direction of initio bcc phase before the shuffle processes among (110) (or $(1-10)$) planes, which generates a strain-free hcp phase when neglecting the slight expansion along $[110]$ (or $[1-10]$ direction). However, the shuffle processes could probably happens in a compressed bcc phase with a compression ratio less than 86.6%, and thus generates a strained hcp phase whose energy is still lower than the compressed bcc phase. Similarly, the shuffle processes may also do not proceed ideally, which will left a shear along the shuffle planes. Though the strained hcp phase is not as stable as an ideal hcp phase in formation energy, misfit energy between the strained hcp nucleus and the surrounding compressed bcc phase is smaller than the one between the ideal hcp nucleus and the bcc phase. If the sum of the formation energy of the hcp phase and the misfit energy reach to a minimum, the transition path is possible and results in a residual strain in the hcp phase. The detailed transition path mainly relies on the strain and strain gradient states of the compressed bcc phase. Ab-initio calculations on the transition path of the phase transition of iron also uncovered the possibility of different transition paths under different pressures albeit with the ideal processes for both the compression and shuffling²⁷. In contrast to the ideal transition path, it may be called “strained transition path”. The strain rate dependence of the strain of bcc phase ahead of the IB (See Fig. 4d) could be explained by the strained transition path. According to the strained transition path, we could infer that c/a ratio, closely related to the strain of the transition product after the transition, also depends on the strain rate, which is consistent with a recent experimental analyses²⁸.

From the physical picture of the wave propagations during ramp compressions, we know that a steady shock wave could form when the speed of NB is equal to that of the IB. Let c_0 to be the speed of the IB, we have

$$v_p = -2\chi_0 dv\lambda_0 + c_0 - c, \quad (5)$$

where c is propagation speed of the strain field. In the above equation, we have taken m to be 1 because the instability region, within the ISF, is too narrow to allow multiple shuffle processes to take place simultaneously. Equation (5) indicates that the compression ratio is linearly related to the particle velocity just ahead of the IB after a steady shock wave forms. As shown in Fig. 4c, the relationship between the compression ratio λ (or linear strain $\varepsilon = \lambda - 1$) and the particle velocity of bcc phase does indeed satisfy equation (5). Assuming that Lagrangian wave speed of the IB is C_L , the relation is equivalent to the simple wave relation, i.e., $dv_p = -C_L d\varepsilon_0$, if $C_L = 2\chi_0 dv$. This is valid if effects of strain rates and dissipative processes, for example, plasticity and phase transition, could be omitted in the equation of states. That is to say, before the instability takes place, an inviscid scalar equation of states is a good approximation for describe single crystalline iron under ramp compressions at low temperature. This is nontrivial because the strain and strain gradient ahead of the IB already become very large and exhibit a nonlinear behavior (See the Supplementary Information).

As shown in Fig. 4d, the formation time of the initial shock could be identified to be 16, 32 and 48ps for the ramp with strain rates of 0.8/5, 0.8/10 and 0.8/15 $\text{\AA}/\text{ps}^2$, respectively. Since the simple wave assumption is valid at until the lattice instability begins, the scaling method proposed by Lane and et. al.²⁹ could be used to explain the difference of the shock-formation time (t_f), that is

$$t_f = t' \frac{v'_{max} t'_{ring}}{v_{max} t_{ring}} = t' \dot{v}'_{max} / \dot{v}_{max} = t' \dot{\epsilon}' / \dot{\epsilon}, \quad (6)$$

where quantities with a upper prime is corresponding to the ones measured in a reference system. Here, we take the reference system to be the simulated iron sample under a ramp compression with $v'_{max} = 0.8$ km/s and $t'_{rising} = 5$ ps, and thus t' , the formation time of the first shock, is about 16ps. Via equation (6), we could infer that the formation time for the ramp compression with $v_{max} = 1.5$ km/s and $t_{rising} = 50$ ps is about 85 ps which is larger than the max allowed wave propagation time in present work (See Fig. 4d). The ratio of the shock-formation time to the ramp rising time is 3.2, about two times of that found in copper³⁰. This is due to the occurrence of the phase transition of iron which results in the forming of the shock in advance. However, we find that the scaling law (6) is also violated when the strain rate is larger than 10^{10} s^{-1} (See the Supplementary Information).

In summary, we find that effects of the strain rates exhibit a certain scaling law at relatively low strain rates, but deviate from the scaling law at extreme strain rates. The deviation is due to emergence of new physical effects caused by the strain gradients under the extreme strain rates. Hence, some new mechanical behaviors in response to the dynamic loadings under the extreme strain rates could be expected.

References

1. Yaakobi B, Boehly TR, Meyerhofer DD, Collins TJB, Remington BA, Allen PG, *et al.* EXAFS Measurement of Iron bcc-to-hcp Phase Transformation in Nanosecond-Laser Shocks. *Physical Review Letters* 2005, **95**(7): 075501.
2. Kalantar DH, Belak JF, Collins GW, Colvin JD, Davies HM, Eggert JH, *et al.* Direct Observation of the alpha - epsilon Transition in Shock-Compressed Iron via Nanosecond X-Ray Diffraction. *Physical Review Letters* 2005, **95**(7): 075502.
3. Milathianaki D, Boutet S, Williams GJ, Higginbotham A, Ratner D, Gleason AE, *et al.* Femtosecond Visualization of Lattice Dynamics in Shock-Compressed Matter. *Science* 2013, **342**(6155): 220-223.
4. Denoeud A, Ozaki N, Benazzimouna A, Uranishi H, Kondo Y, Kodama R, *et al.* Dynamic X-ray diffraction observation of shocked solid iron up to 170 GPa. *Proceedings of the National Academy of Sciences* 2016.
5. Boettger JC, Wallace DC. Metastability and dynamics of the shock-induced phase transition in iron. *Physical Review B* 1997, **55**(5): 2840.
6. Jensen BJ, Gray IGT, Hixson RS. Direct measurements of the α - ϵ transition stress and kinetics for shocked iron. *Journal of Applied Physics* 2009, **105**(10): 103502.
7. Zarkevich NA, Johnson DD. Coexistence pressure for a martensitic transformation from theory

- and experiment: Revisiting the bcc-hcp transition of iron under pressure. *Physical Review B* 2015, **91**(17): 174104.
8. Caspersen KJ, Lew A, Ortiz M, Carter EA. Importance of Shear in the bcc-to-hcp Transformation in Iron. *Physical Review Letters* 2004, **93**(11): 115501.
 9. Barge NV, Boehler R. Effect of non-hydrostaticity on the α - ϵ transition of iron. *High Pressure Research* 1990, **6**(2): 133-140.
 10. Ma Y, Selvi E, Levitas VI, Hashemi J. Effect of shear strain on the α - ϵ phase transition of iron: a new approach in the rotational diamond anvil cell. *Journal of Physics: Condensed Matter* 2006, **18**(25): S1075.
 11. Born M, Huang K. *Dynamical Theory of Crystal Lattices*. Oxford university press: London, 1988.
 12. Grimvall G, Magyari-Köpe B, Ozoliņš V, Persson KA. Lattice instabilities in metallic elements. *Reviews of Modern Physics* 2012, **84**(2): 945.
 13. Kadau K, Germann T, Lomdahl P, Holian B. Atomistic simulations of shock-induced transformations and their orientation dependence in bcc Fe single crystals. *Physical Review B* 2005, **72**(6): 064120.
 14. Crowhurst JC, Reed BW, Armstrong MR, Radousky HB, Carter JA, Swift DC, *et al.* The $\alpha \rightarrow \epsilon$ phase transition in iron at strain rates up to 10^9 s^{-1} . *Journal of Applied Physics* 2014, **115**(11): 113506.
 15. Smith RF, Eggert JH, Swift DC, Wang J, Duffy TS, Braun DG, *et al.* Time-dependence of the alpha to epsilon phase transformation in iron. *Journal of Applied Physics* 2013, **114**(22): -.
 16. Amadou N, de Resseguier T, Brambrink E, Vinci T, Benuzzi-Mounaix A, Huser G, *et al.* Kinetics of the iron alpha-epsilon phase transition at high-strain rates: Experiment and model. *Physical Review B* 2016, **93**(21): 214108.
 17. Smith RF, Eggert JH, Rudd RE, Swift DC, Bolme CA, Collins GW. High strain-rate plastic flow in Al and Fe. *Journal of Applied Physics* 2011, **110**(12): -.
 18. Smith R, Eggert J, Jeanloz R, Duffy T, Braun D, Patterson J, *et al.* Ramp compression of diamond to five terapascals. *Nature* 2014, **511**(7509): 330-333.
 19. Coppari F, Smith RF, Eggert JH, Wang J, Rygg JR, Lazicki A, *et al.* Experimental evidence for a phase transition in magnesium oxide at exoplanet pressures. *Nature Geosci* 2013, **6**(11): 926-929.

20. Wang J, Coppari F, Smith RF, Eggert JH, Lazicki AE, Fratanduono DE, *et al.* X-ray diffraction of molybdenum under ramp compression to 1 TPa. *Physical Review B* 2016, **94**(10): 104102.
21. Seagle CT, Davis JP, Martin MR, Hanshaw HL. Shock-ramp compression: Ramp compression of shock-melted tin. *Applied Physics Letters* 2013, **102**(24).
22. Jue W, Smith RF, Eggert JH, Braun DG, Boehly TR, Reed Patterson J, *et al.* Ramp compression of iron to 273 GPa. *Journal of Applied Physics* 2013, **114**(2): 023513 (023518 pp.)-023513 (023518 pp.).
23. Amadou N, Brambrink E, Benuzzi-Mounaix A, Huser G, Guyot F, Mazevet S, *et al.* Direct laser-driven ramp compression studies of iron: A first step toward the reproduction of planetary core conditions. *High Energy Density Physics* 2013, **9**(2): 243-246.
24. Morard G, de Rességuier T, Vinci T, Benuzzi-Mounaix A, Lescoute E, Brambrink E, *et al.* High-power laser shock-induced dynamic fragmentation of iron foils. *Physical Review B* 2010, **82**(17): 174102.
25. Wang K, Xiao S, Deng H, Zhu W, Hu W. An Atomic Study on The Shock-Induced Plasticity and Phase Transition for Iron-based Single Crystals. *International Journal of Plasticity* 2014, **59**(0): 180-198.
26. Dupé B, Amadon B, Pellegrini Y-P, Denoual C. Mechanism for the $\alpha \rightarrow \epsilon$ phase transition in iron. *Physical Review B* 2013, **87**(2): 024103.
27. Lu Z, Zhu W, Lu T, Wang W. Does the fcc phase exist in the Fe bcc–hcp transition? A conclusion from first-principles studies. *Modelling and Simulation in Materials Science and Engineering* 2014, **22**(2): 025007.
28. Konôpková Z, Rothkirch A, Singh AK, Speziale S, Liermann H-P. In situ x-ray diffraction of fast compressed iron: Analysis of strains and stress under non-hydrostatic pressure. *Physical Review B* 2015, **91**(14): 144101.
29. Lane JMD, Foiles SM, Lim H, Brown JL. Strain-rate dependence of ramp-wave evolution and strength in tantalum. *Physical Review B* 2016, **94**(6): 064301.
30. Higginbotham A, Hawreliak J, Bringa EM, Kimminau G, Park N, Reed E, *et al.* Molecular dynamics simulations of ramp-compressed copper. *Physical Review B* 2012, **85**(2): 024112.

Acknowledgements

This work is supported by the National Natural Science Foundation of China (NSFC-NSAF 11076012 and NSFC 11102194, 11402243), National Key Laboratory Project of Shock Wave and Detonation Physics (No. 077120), the Science and Technology Foundation of National Key Laboratory of Shock Wave and Detonation Physics (Nos. 9140C670201110C6704 and 9140C6702011103) and Chinese National Fusion Project for ITER with Grant No. 2013GB114001.

Author contributions

K.W. performed the MD simulations, developed the theory, carried out code development (the lattice dynamic analyses) and wrote the paper; J.C. and W.Z. originated the central idea; W.H. and M. X. contributed in manuscript editing. All contributed to discussions.

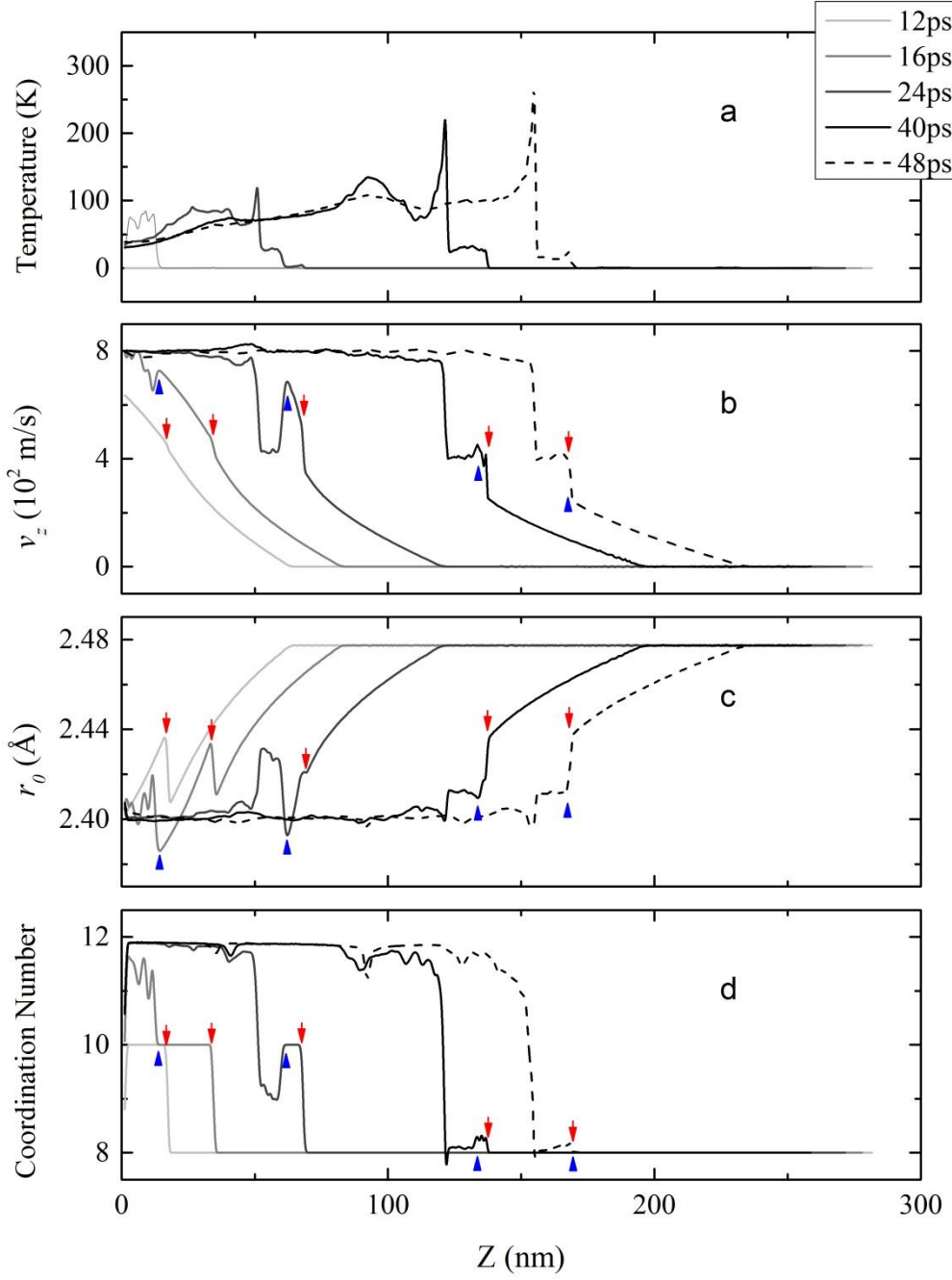


Fig. 1. Profiles represented by (a) temperature, (b) particle velocity, (c) nearest neighbor separation and (d) coordination number of iron samples under ramp compression along [001] direction with a max particle velocity of 0.8 km/s and a ramp rising time of 15ps. The first kink in each profile (marked by a downward red triangle above each profiles) is caused by the transition from bcc phase to the TCN structure, which indicates the onset of lattice instability. Phase transition proceeds in the unstable region. Positions of the NB at each moment are marked by an upward blue triangle below the corresponding profiles.

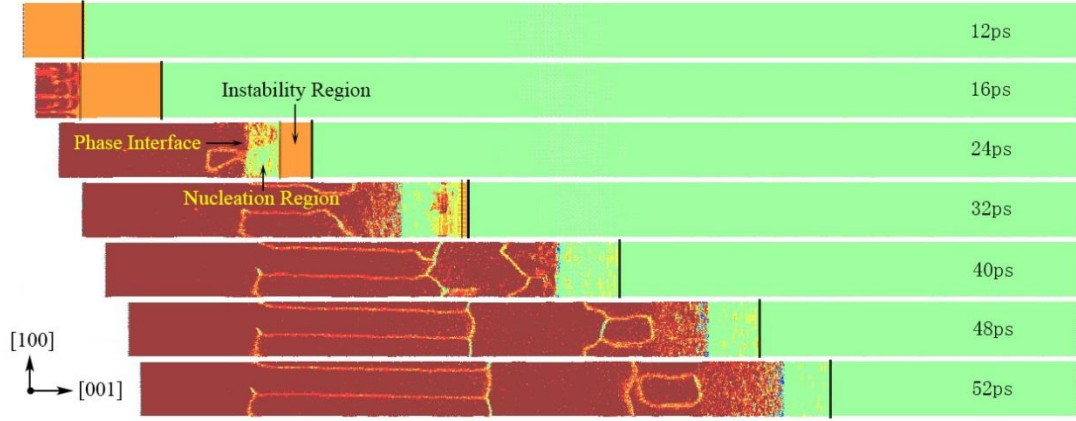


Fig. 2. Phase evolutions of the simulated iron sample during ramp compression with an applied strain rate of $8/15 \text{ \AA/ps}^2$. All snapshots of the simulated sample at each moment are colored by coordination number of atoms: dark blue (12), light blue (11), green (10), yellow (9), and red (8), where compression waves propagate from left to right. The instability interface (or phase interface) is marked by a gray (black) bar in each snapshot. The unstable region disappears from the wave profiles when the phase interface catch up to the instability interface. A mixed-phase region emerges before a complete transition from the bcc phase to the hcp phase.

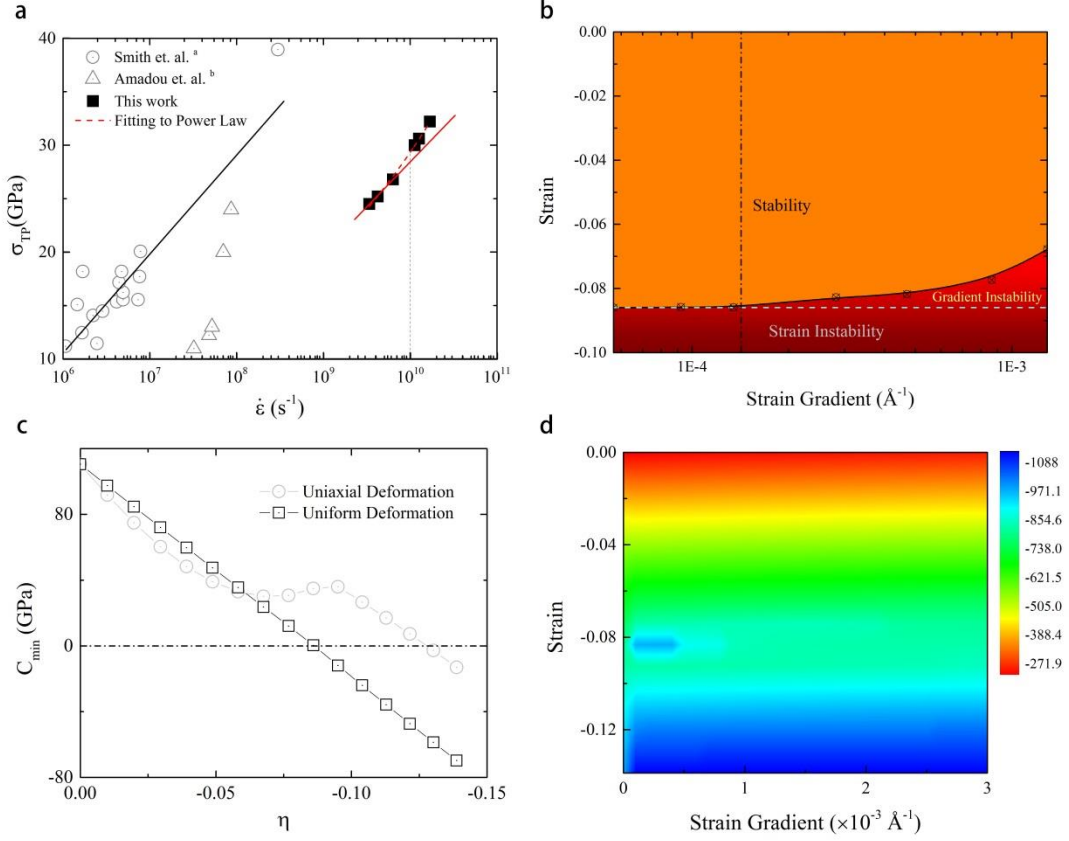


Fig. 3. (a) The transition pressure of iron as a function of uniaxial strain rate, represented by $\log \dot{\epsilon}$. The red dashed line is fitted to a power law of $\sigma_{TP} = A_0 \dot{\epsilon}^n$, where $A_0 = 0.53$, $n = 0.17$. Alternatively, we find that the power law is equivalent to a scaling law of $\sigma_{TP} = \sigma_0 (\dot{\epsilon}/\dot{\epsilon}_0)^n$, where σ_0 are a reference TP under a strain rate of $\dot{\epsilon}_0$. Systematic errors emerging in the fitting indicate that there is a different law existing beyond $10^{10} s^{-1}$, which stems from the effects of strain gradient. Two different laws are marked by red dashed and red solid line, respectively. (b) Strain, as well as strain gradient, at the onset of the instabilities during ramp compressions with different max particle velocities and ramp rising times, covering the onset of the phase transition of bcc iron, which forms an boundary (denoted by the black line) departing stable region from unstable region. The horizontal dashed line is corresponding to a critical strain (-0.086) predicted by the modified B criteria (See Fig. 5), which gives a plausible explanation at low strain gradient. However, the critical strains depart from the predicted value at large strain gradients. (c) Minimum eigenvalue of elastic constants of bcc iron as a function of volume strain and uniaxial strain, respectively. The critical strain is -0.086 and -0.128 under uniform deformations and uniaxial deformations, respectively. (d) \tilde{T}_{min} as a plot of uniaxial strain and uniaxial strain gradient for single crystalline iron, where the unit is $\text{GPa} \cdot \text{\AA}^2$.

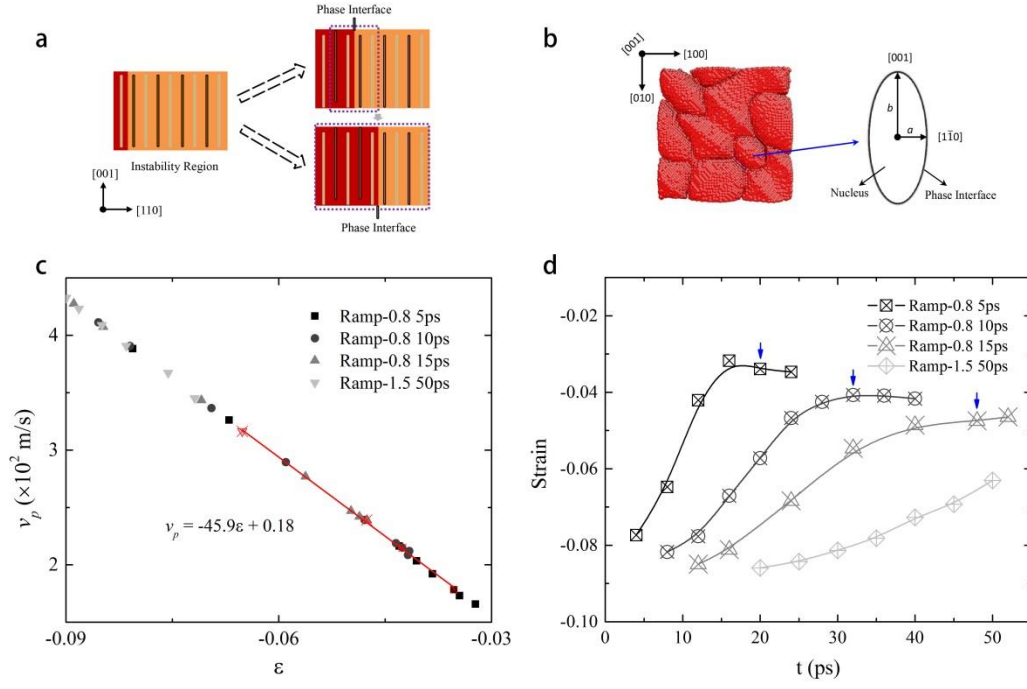


Fig. 4. (a) Schematic drawing of the propagation of the phase interface and the instability interface during ramp compressions, whose reference frame moves at a speed equal to that of the instability interface. In considering the shuffle planes of the phase transition for the shock along [001] direction, the long bars in the sample denote (110) (or $(1\bar{1}0)$) planes of bcc iron. The transition wave is assumed to propagate along [110] (or $[1\bar{1}0]$) direction which is normal to the [001] direction. The region nearby the phase interface, circled by the dashed square, represents a spatial range affected by the phase interface. Two different spatial ranges correspond to the two growth modes as marked by the dashed arrows, respectively. (b) Nucleation of hcp phase at 16ps under ramp compressions with a strain rate of $8/15 \text{ \AA/ps}^2$ and a schematic drawing of an hcp nucleus (marked by the blue arrow). (c) Particle velocity as a function of strain ahead of the IB for different ramp compressions, where the strains, at the moment when the initial shock forms, are marked by the red crosses. The red line is a linear fitting to the marked strains, whose fitting expression has been shown in the figure. (d) Time evolution of the strain ahead of the IB. The blue arrows mark the time when the initial shock forms.